IEEE Access
Multidisciplinary | Rapid Review | Open Access Journal

Received January 4, 2022, accepted January 19, 2022, date of publication January 26, 2022, date of current version February 4, 2022.

Digital Object Identifier 10.1109/ACCESS.2022.3146386

A Wearable Circularly Polarized Antenna Backed by AMC Reflector for WBAN Communications

YOUCEF BRAHAM CHAOUCHE[1,2], (Graduate Student Member, IEEE), MOURAD NEDIL[1], (Senior Member, IEEE), ISMAIL BEN MABROUK[3], (Senior Member, IEEE), AND OMAR M. RAMAHI[2], (Fellow, IEEE)

[1]Underground Communications Research Laboratory, Engineering School, University of Quebec at Abitibi-Temiscamingue (UQAT), Val d'Or, QC J9P 1Y3, Canada
[2]Department of Electrical and Computer Engineering, University of Waterloo, Waterloo, ON N2L 3G1, Canada
[3]Department of Engineering, Durham University, Durham DH1 3LE, U.K.

Corresponding author: Youcef Braham Chaouche (youcef.brahamchaouche@uqat.ca)

This work was supported in part by the Centre for Systems, Technologies and Applications for Radio frequency and Communication (STARaCom), Fonds québécois de la recherche sur la nature et les technologies (FRQNT), QC, Canada.

ABSTRACT A new flexible circularly polarized (CP) wearable antenna is proposed for Wireless Body-Area Network systems (WBAN) operating at 5.8 GHz. The circular polarization is enabled by combining a microstrip-line monopole feed and an inverted L-shaped conformal metal strip extended from a coplanar waveguide. The proposed antenna shows satisfactory performance in terms of gain and specific absorption rate (SAR) at a separation of 12 mm from a human body model. To minimize body-antenna separation, a flexible 2 × 2 artificial magnetic conductor (AMC) was used as a reflector to achieve good performances in terms of gain and SAR. The total footprint of the proposed antenna is only 34.4 × 34.4 mm^2 (0.384 λ_0^2) board of semi-flexible Rogers RT-Duroid 5880 substrate. The final design provides a peak gain of 7.6 dBi and an efficiency of 94.7% when worn on the body. Furthermore, evaluation results indicate that the maximum SAR level decreased by up to 20.42% in comparison with the CP antenna without the AMC. Full-wave EM simulation and experimental results are performed, both in free space and proximity to the human body under different bending scenarios. Overall, the proposed antenna performance has been shown to be robust to structural deformation along the x-axis in comparison to previously reported designs. These features demonstrate that the proposed antenna is a strong candidate for off-body wearable applications.

INDEX TERMS Wireless body area network, wearable antenna, off-body communication, circular polarization, artificial magnetic conductor (AMC).

I. INTRODUCTION

Recently, the interest in wireless body area networks (WBANs) has been rising significantly in the development of flexible and wearable devices [1]. Additionally, antennas integrated into wearable devices have attracted strong interest due to their diverse applications in the personal entertainment, health care, and defense sectors [2]. Moreover, due to the growth in wireless sensors in biomedical applications, the demand for high-performance compact flexible wearable antennas has dramatically increased, particularly those capable of supporting efficient off-body communications [3]. Since wearable antennas operate within the vicinity of the body, the loading effect of lossy tissue and structural deformation such as bending and crumpling, must be considered in the antenna design process [4]. Furthermore, wearable antennas are subject to several shape distortions due to the uncertain form of the material surface during the wearer's daily activities.

As a result, the scattering due to the body motion can modify the reflected polarization of the wave, causing polarization disparity [5]. Thus, wearable antennas with robust performance that solve problems in terms of influence of the lossy dielectric human tissue body, deformation, and polarization mismatch, are suggested for WBAN applications [6].

Several off-body communication antennas, with and without the integration of flexible/textile materials, have been proposed for wearable applications in the 2.4/5.8 GHz

The associate editor coordinating the review of this manuscript and approving it for publication was Xujie Li.

industrial, scientific, and medical (ISM) bands. Patch antennas [7], planar monopoles [8], and slot antennas [9], have been proposed for conventional wearable antennas applications. Hence, various antenna designs have been also introduced to achieve enhanced performance and provide multiple functionalities [10]–[16]. Specifically, slot antennas based on substrate integrated waveguide (SIW) technology, exhibiting either single or dual-band operation, have been discussed in [10]–[12]. Similarly, fractal [13], [14], inverted-F [15], and textile antennas [16] have also been suggested to improve SAR levels when placed in close proximity to the human body.

On the other hand, to minimize the human body effect, an isolating layer is used as a backing shield to the wearable antenna such as artificial magnetic conductor (AMCs) [17], [18], electromagnetic bandgap (EBG) [19], [20], high impedance surfaces (HISs) [21], [22], and electric ring resonators (ERRs) [23]. Therefore, radiation patterns toward the human body surface are reduced with good improvements in terms of gain and front-to-back ratio (FBR) are achieved [24], [25]. It is noticed that most of the above-mentioned antennas are linearly polarized (LP), which could result in a limitation for the function activities due to the polarization mismatch losses caused by the human body movements. The use of wearable circularly polarized (CP) antenna is the best way to mitigate this problem. For instance, a compact circularly polarized (CP) integrated filtering antenna is reported in [26] for wearable biotelemetric devices. In [27], a circularly polarized button antenna for 5 GHz WBAN applications has been studied. A compact and high-efficiency CP antenna for body-centric applications has been reported in [28]. However, the most reported CP antennas applied for WBAN applications are based on rigid substrates, which cannot exhibit conformal characteristics. In this area, few research works on CP wearable antennas have been reported [29]–[32]. The multilayer flexible CP antenna is introduced in [29]. In [30], a costly CP antenna has been suggested by using flexible polydimethylsiloxane (PDMS) as a substrate. In [31], a bulky circularly polarized wearable DRA has been also investigated for off-body communication. In addition, a wearable textile CP antenna was designed in [32] for location tracking purposes. Significant frequency shifts occur due to structural deformation resulted in an increase of beam width with a decrease in the gain. Moreover, these antennas have characteristics in common that limit performance, such as low efficiency, narrow bandwidth, frequency shifts, and poor front-to-back ratio (FBR) under different bending conditions, and their complex excitation mechanism made the design uncomfortable to the user. Therefore, a flexible CP antenna with significant performance and bending robustness capabilities are highly desirable for integrating into wearable devices.

In this paper, a flexible CP wearable antenna backed by an AMC array structure is designed and investigated for WBAN applications. The proposed antenna consists of a coplanar waveguide (CPW)-fed microstrip line monopole antenna.

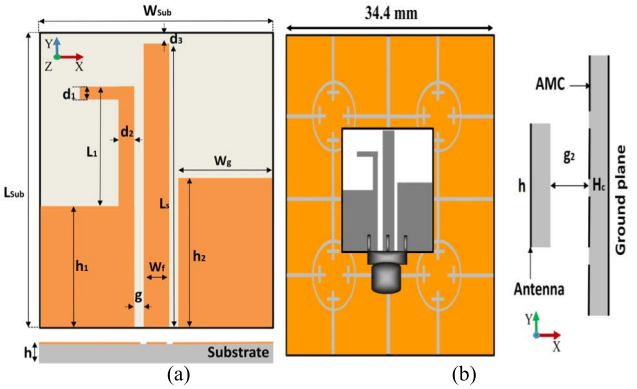

FIGURE 1. (a) 2D Layout geometry of the proposed CP antenna, (b) Integrated design layout modeled on CST. With $g_2 = 3$ mm.

An inverted L-shape parasitic strip from one side of the coplanar ground planes has been designed to achieve the CP capability at 5.8 GHz. Moreover, the monopole antenna is backed by a compact 2 × 2 AMC array, to reduce the backward electromagnetic radiation towards the human body. The proposed antenna system is thinner than the earlier reported ones. Besides, it provides good performances in terms of SAR and gain. The antenna has been fabricated and tested when placed in different places of the human body, with considering different bending scenarios.

The remainder of this paper is structured as follows: Section II describes the antenna design. Section III deals with the implementation of the antenna with a novel array of periodic AMC model. Section IV analyzes the effects of human body loading on the performance of the integrated antenna under various scenarios, including antenna properties, and SAR levels. Summary and Conclusions are given in section V.

II. ANTENNA DESIGN AND ANALYSIS

In this section, the design process of the proposed CP antenna is investigated. In addition, numerical simulations and experimental data of S parameters, total efficiency, realized gain, and radiation patterns are examined.

A. ANTENNA DESIGN

In this study, the targeted application is specifically designed to operate at 5.8 GHz of the ISM band which can easily fit any wearable and conformal wireless device. The application is intended for health monitoring of medical status via wearable sensors, which is placed on a different human body part. The antenna topology consists of a coplanar waveguide CPW-fed CP monopole antenna with dimensions of $L_s \times W_s$. The antenna dimensions are determined in free space wavelength at the lowest operating frequency. The antenna is developed on the front of a single layer of 0.508 mm semi-flexible RT/duroid 5880 substrate, with relative permittivity of 2.2, and tangent loss of 0.0009, as shown in Fig. 1. The antenna is fed using a 50 Ω CPW to provide good impedance

matching. The proposed CP-antenna is designed by integrating an inverted L-stub extended from one side of the CPW ground plane in the front of the microstrip line. To improve the AR over the wideband, the width of the coplanar ground plane is considered to obtain two components of an electric field in both orthogonal x and y directions.

B. ANTENNA EVOLUTION

In this step, the design procedure is discussed to generate circular polarization by using coplanar strip (CS) based excitation technique. These technologies are characterized by easy realization, balanced circuit, and reduced crosstalk between the lines. For both asymmetric CPW and CS, closed-form expressions for the effective dielectric constant and characteristic impedance of the asymmetric CPW were derived using conformal mapping methods reported in [33].

In fact, the proposed topology underwent several development stages evolutions steps to achieve the final proposed structure as illustrated in Fig. 2. In the first step, a CPW-fed rectangular slot antenna is printed on the substrate. The length of the microstrip monopole is 13.9 mm, which is approximately a quarter wavelength at the lower cutoff frequency (referred to Ant.1). Fig. 3 shows the relevant antenna characteristics corresponding to the stages of Fig. 2. The impedance matching characteristic at stage 1 shows a resonance near 9 GHz, which is due to the quarter-wavelength monopole. The AR response shows that the antenna is somewhat CP, which is attributed to the symmetrical topology of the CPW.

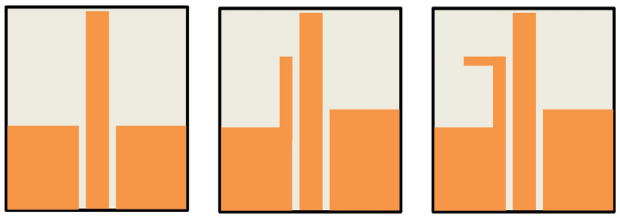

FIGURE 2. Evolution prototypes of the proposed antenna: (a) Ant.1, (b) Ant.2, (c) Ant.3.

At the second stage, a stub is added within the coplanar ground plane to the left of the transmission line to create additional electric field component along the Y-direction and generate CP radiation [34]. Moreover, to merge the CP waves at the upper and the lower bands, the dimension of the right coplanar ground plane was adjusted in they-direction. When CPW is used with a symmetric ground plane, the current directions on the edges of the ground plane are opposite to each other and, hence, cancel out in the far-field as the waves radiated by the ground plane are out of phase. As a result, the impedance bandwidth shows a clear improvement (referred to Ant.2). On the other hand, the AR response related to the stage 2 [see Fig. 3(b)] is also improved, which is due to the induction of the additional electric E-field component along L_1, d_2 and h_2 [See Fig. 1(a)]. In addition, the antenna reflection coefficient shows a resonance at 5.93 GHz with an impedance bandwidth of 5.71-6.3 GHz in the case of Ant.2 [see Fig. 3(a)]. Also, the optimum AR frequency $\leq$3 dB [see (Fig. 3(b)] is found to be wider at 6 GHz (5.86-9.05 GHz).

In order to improve the S_{11} and AR performances, the current stub path of 2.8 mm is extended to create inverted L-strip in the -Y direction. As a result, a further electric field, with equal magnitude and 90° phase difference, is created to generate CP characteristic, as illustrated in Fig. 2(c) (referred to Ant.3). It is worth mentioning that using the excitation technique based on coplanar strip (CS) and asymmetric CPW, the fundamental vertical and horizontal components for the CP are generated with maintaining compact and structurally simple antenna with wide 3 dB AR bandwidth. Based on the above discussion, Table 1 propose the following design guidelines for the different design stages.

TABLE 1. Overview of the design guidelines [35].

Design Guidelines	Design No.	Step	Procedure
For wideband	Design 1	1	Design a CPW-fed rectangular slot antenna with a 50 Ω microstrip feed line. In this stage Ls is the key parameter to control the resonant frequency.
For circular polarization	Design 2	2	A stub is extended within the coplanar ground plane to the left of the transmission line. Hence, the symmetry of the CPW is slightly broken, which creates additional electric field component along the Y-direction resulting in generating CP radiation capability.
Design improvements	Design 3	3	To further improve the impedance matching and AR, the current path is lengthened by extending the stub to create inverted L-strip in the -Y direction.

The optimized results are shown in Fig. 3. Moreover, a wideband from 5.44 to 6.24 GHz is achieved in case of Ant.3. The simulation at this stage indicates a broadband CP characteristic from 5.27 to 8.65 GHz. The final optimized parameters are summarized in Table 2. All theoretical design phases in this study have been simulated using Computer Simulated Technology (CST) 2020 [36].

TABLE 2. Optimised dimensions of the proposed antenna.

Parameter	Value (mm)	Parameter	Value (mm)
h_1	5.6	W_{sub}	13
L_1	6.4	L_{sub}	14
d_1	0.5	h_2	7
d_2	1	W_f	1.9
d_3	0.1	W_g	5.3
L_s	13.9	g	0.2

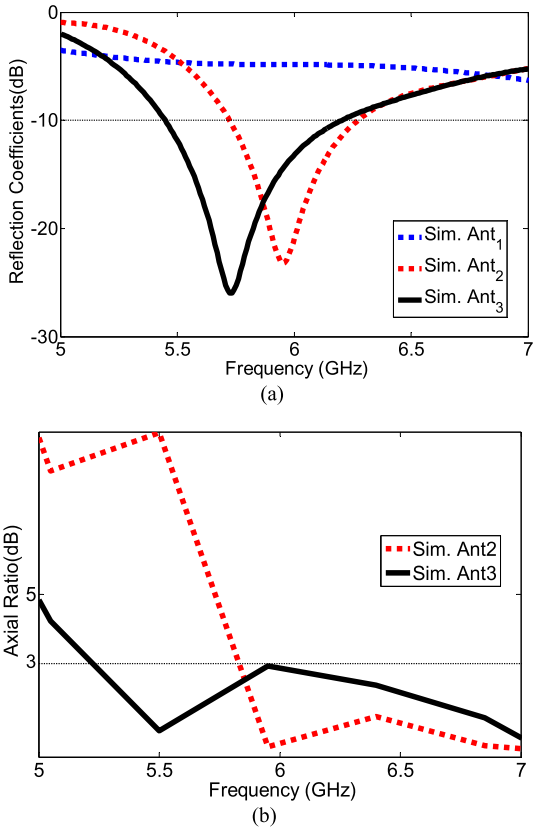

FIGURE 3. Comparison of different monopole antennas: (a) S_{11}, (b) AR.

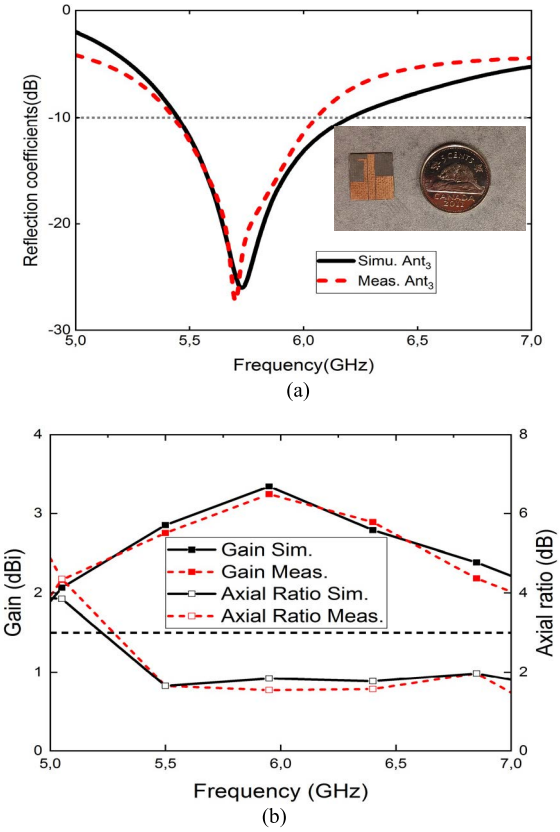

FIGURE 4. Simulated and measured results of the fabricated prototype. (a) Reflection coefficient, (b) Efficiency and gain.

Fig. 4(a) shows the measured reflection characteristics of the proposed antenna with the help of calibrated ANRITSU MS4647A Vector Network Analyzer (VNA). The antenna design displayed a simulated wide-band resonance ranging from 5.44-6.24 GHz, whereas the measured result achieved a bandwidth ranging from 5.45 to 6.06 GHz. The simulated and measured gain is shown in the left y-axis scale of Fig 4(b). The realized gain varied from 2.9 to 3.4 dBi (a gain of 3.3 dBi is observed at 5.8 GHz).

Similarly, the simulated and measured AR bandwidth of the proposed antenna, showed features of 48.56% of circular polarization axial ratio bandwidth when simulated, and 45.4% when measured. Good agreement can be observed between measurements and simulated results in terms of S_{11} and AR, respectively.

Regarding the circular polarization radiation mechanism, further analysis has been performed. Fig. 5 illustrates the simulated electric surface current distribution on the monopole antenna at 5.8 GHz for phases 0°, 90°, 180°, and 270°. As shown in Fig. 5(a), most of the current is concentrated in +y direction in the case of 0° phase reference.

For the 90° phase reference (see Fig. 5(b)), the dominant field is predominantly in -x-direction at the edge of the ground plane. At 180° and 270° phases, the fields are seen to have the same magnitudes but opposite orientation phases,

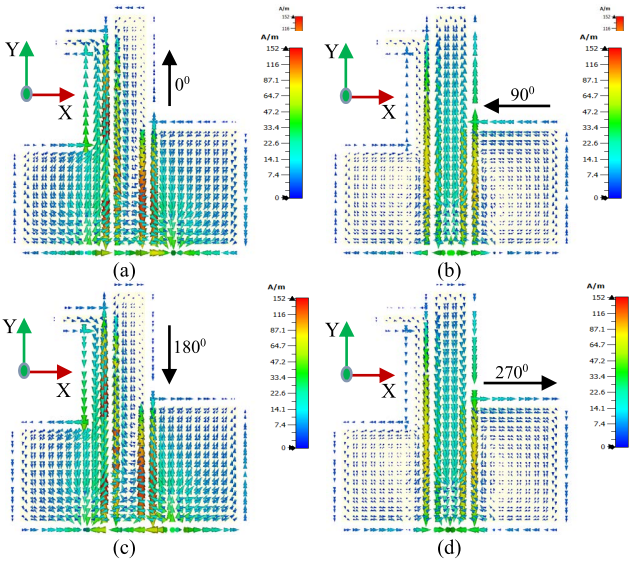

FIGURE 5. Simulated electric surface current distribution of the proposed antenna at 5.8 GHz. (a) 0°. (b) 90°. (c) 180°. (d) 270°.

with respect to those at 0° and 90° phases. Consequently, since the current circulates in the counterclockwise direction, the LHCP and RHCP characteristics are achieved (see Fig. 5(c)-(d)).

Fig. 6 shows the radiation patterns of the proposed antenna in free space including RHCP and LHCP, in both xz ($\varphi = 0°$) and yz ($\varphi = 90°$) plane. From these results, a stable unidirectional radiation pattern is obtained with a maximum gain of 3.3 dBi at 5.8 GHz. Furthermore, a good agreement between simulations and measurement results is observed.

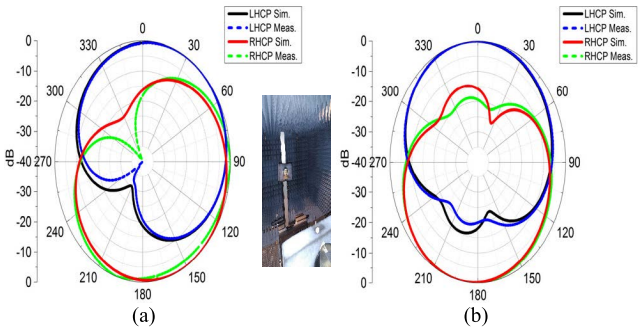

FIGURE 6. Comparison between simulated and measured polar plot representation of the radiation pattern. (a) $\varphi = 0°$, (b) $\varphi = 90°$.

III. ANTENNA AMC-BACKED DESIGN

A. AMC DESIGN

Fig. 7(a) depicts the proposed unit-cell geometry of the AMC plane. The designed unit-cell is based on parasitic elements' technique suggested for wideband structures [37]. This new concept consists of circular symmetric patches coupled by arms located at the center. It is realized on a semi-flexible RO5880 substrate with a thickness of $H_c = 0.508$ mm, a relative permittivity of $\varepsilon_r = 2.2$, and loss tangent of $\tan\delta = 0.0009$. By adjusting the length of arms (d_2) and slots on the patch (W_g), the reflection phase bandwidth of the proposed AMC design can be easily controlled. The boundary condition of the AMC unit-cell structure is illustrated in Fig. 7(b). To simulate the reflection phase with a periodic boundary condition, each of facing walls are set to be identical to the PEC (perfect electric conductor) and the PMC (perfect magnetic conductor). The wave-port is used to simulate the reflection phase on the surface of the unit cell. The desired frequency is calculated based on equation (1) [38].

$$f_r = \frac{1}{2\pi\sqrt{LC}} \tag{1}$$

where L is the equivalent inductance and C is the capacitance associated with the periodic unit cell. From equation (1), it can be noticed that, with an increment of the inductance or the capacitance of the unit-cell, the resonance frequency will shift to the lower band. In addition, the bandwidth will decrease while increasing the capacitance. Hence, it is preferable to increase the inductance instead of the capacitance of the unit cell. In fact, the inductance can be increased without increasing the capacitance by using a thick substrate. In this case, the resonant frequency (f_r) corresponding to the effective equivalent circuit model depicted in Fig. 7(c) can be expressed as [38].

$$f_r = \frac{1}{2\pi\sqrt{(L_g + L_d)\, C_g}}, \tag{2}$$

where L_g and L_d are the grid inductances and the dielectric slab inductance, respectively. The grid capacitance C_g is the gap size between two parallel patches that can be expressed by (3) [38].

$$C_g = \frac{W\varepsilon_0\,(1+\varepsilon_r)}{\pi}\cosh^{-1}\left(\frac{a}{g}\right), \tag{3}$$

where W is the AMC unit-cell width, g is the gap between two adjacent unit-cells, and $a = 2s + g$, where s is the length of the unit-cell slots. Hence, the bandwidth of the AMC unit-cell can be extracted using (4):

$$BW = \frac{\pi}{8\eta_0}\sqrt{\frac{L_d + L_g}{C_g}} \times \left(\frac{L_d}{L_d + L_g}\right)^2 \tag{4}$$

Fig. 7(d) shows the fabricated AMC array. The proposed design can be further miniaturized by increasing one of the following design parameters: L_d, L_g, C_g. In fact, enhancing L_d leads to a higher profile, which is not desired for wearable applications. It is noticed from equation (2) that adding slots and parasitic patches in the AMC geometry, leads to modify the current path which increases the grid inductance L_g.

In another word, further miniaturization can be achieved by increasing the grid capacitance (C_g) which can be performed by either increasing the length of slot to gap ratio (a/g) or through dielectric loading. A suitable choice of s and g leads to an increase in the (a/g) ratio as described in (3). The inductive and capacitive effects of notches on the four corners play a prominent role in achieving broad bandwidth. Besides, the bandwidth enhancement of the AMC unit-cell design is obtained by increasing L_g and decreasing C_g allowed by the arm and the parasitic patch effects. In order to help figure out the impact of the equivalent circuit.

This phenomenon could be observed by analyzing the surface current magnitude of the proposed unit cell at 5.8 GHz, as shown in Fig. 8. As observed, the maximum concentrated current density is mainly located along with the slot of the ring and is symmetrically distributed between the parasitic arms. This is due to the fact that by inserting the slots, the capacitive and inductive coupling enhance the AMC bandwidth. Hence, the incorporated slots can control the resonant frequency and improve the AMC unit-cell performance. In addition, as the number of slots increases, maximum current is achieved.

On the other hand, the influence of the AMC design parameters is investigated to describe how the different constitutive parts affect the mechanism of the bandwidth enhancement. It can be observed from Fig. 9 that increasing s leads to shift the reflection phase (from 5.2 to 5.95 GHz). Similarly, when s is decreased, the reflection phase is also affected (Fig. 9(a)).

Moreover, by varying the radii of the big circle ring, r_1, and the small ring, r, the reflection phase of the AMC cell

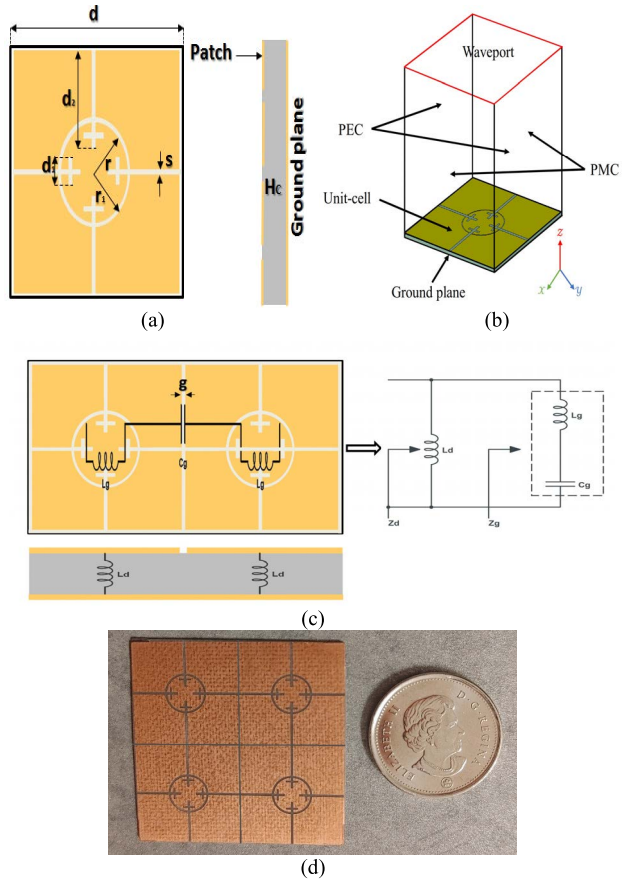

FIGURE 7. (a) Layout of the AMC unit cell. (b) Boundary condition. (c) Equivalent circuit model. (d) Fabricated prototype. (d = 17.2mm, r = 3.2mm, r_1 = 3.3mm, d_1 = 2mm, S = 0.4mm, d_2 = 7.4mm, H_c = 0.508mm, g = 0.1 mm).

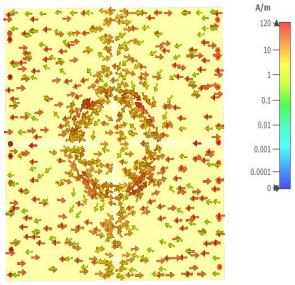

FIGURE 8. AMC unit cell surface current distribution at 0° (5.8 GHz).

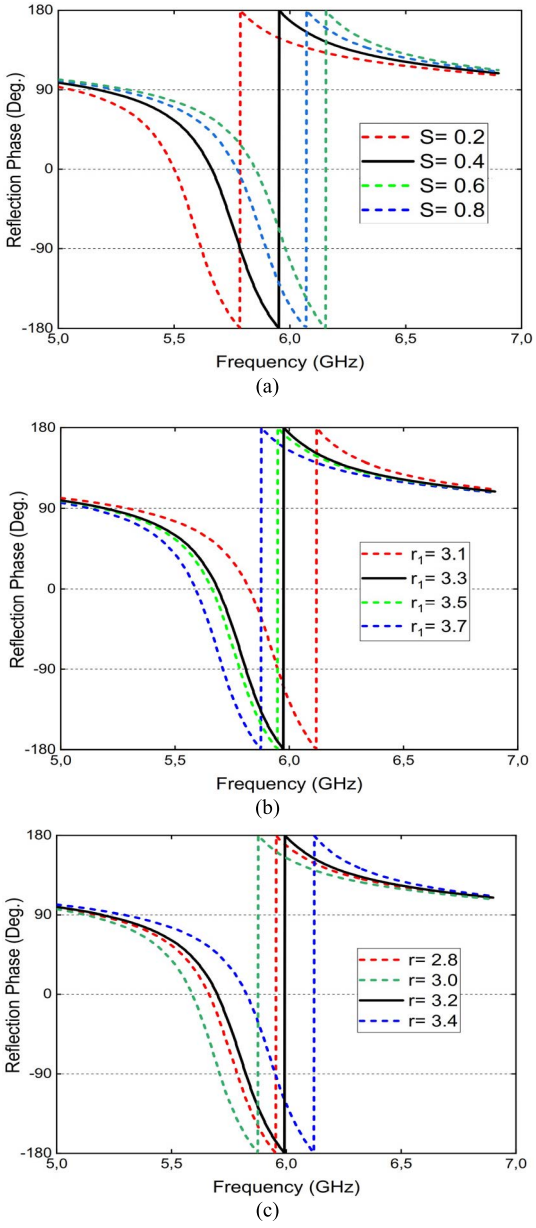

FIGURE 9. Parametric analysis of the AMC unit-cell in terms of phase reflection.

changes dramatically (Fig. 9(b)-(c)). While the values of r_1 are set as 3.1, 3.3, and 3.5 mm, the zero-phase of the reflection coefficient will occur at 5.65, 5.7, and 5.72 GHz, respectively. While r changes from 2.8 to 3.4 mm (in steps of 0.2 mm), the operation frequency of the unit cell decrease gradually from 5.65 to 5.85 GHz.

Based on the theoretical analysis, the reflection phase performances of the unit-cell layout and the equivalent circuit model are presented in the left-hand scale of Fig. 10(a). A good agreement is observed from both computations, where 0° reflection phase is reached at 5.7 GHz, with a bandwidth of 5.17 to 5.82 GHz (±90° reflection phase). On the other hand, the right-hand scale of Fig. 10(a) illustrates the high impedance feature of the AMC unit-cell, where an impedance of 16.5 KΩ is obtained. Moreover, the dispersion diagram is depicted in Fig. 10(b), where a surface wave bandgap is located between 4.2 and 6 GHz, where the AMC zero reflection frequency at 5.7 is exhibited.

In the case of the integrated design, the angular stability of the AMC will influence the antenna radiation performance [39]. Therefore, this particular AMC surface was selected as a candidate for the antenna application in this work, which requires good angular stability. The reflection phase versus frequency plot for different polarization angles

θ (0° to 45°), under various TE and TM oblique incidence of $\varphi = 0°$ and $\varphi = 90°$ is displayed in Fig. 11. As observed, the obtained results of TE and TM polarized waves have no significant difference. It can be noticed that the wide bandwidth of the proposed AMC design is obtained in the different polarization angles of θ for various incident angles.

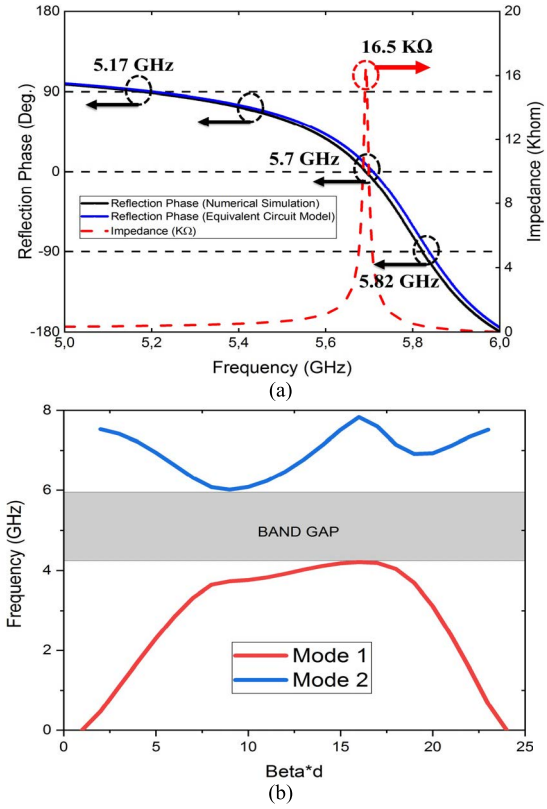

FIGURE 10. (a) AMC unit cell reflection phase and impedance performances. (b) AMC unit-cell dispersion diagram.

From these results, it can be shown, from Fig. 11(a)-(b), that the proposed unit cell is highly stable as its angular margin ranges from 0° to 45°, thus preserving an AMC operation bandwidth of 650 MHz. It is worth mentioning that due to the symmetric design of the AMC unit cell, the results of reflection phase are similar in both polarization angles of $\varphi = 0°$ and $\varphi = 90°$.

B. INTEGRATED DESIGN AND FREE SPACE RESULTS ANALYSIS

The block diagram of the far-field measurement setup and actual setup inside an anechoic chamber is illustrated in Fig. 12(a)-(b). The phase of the two field components is measured relative to the signal generator, and a rectangular horn (high linear polarization purity) serves as the source antenna. A major source of measurement errors should be eliminated, since rectangular horn antennas generate lower levels of cross-polarization over broad bands compared to circular polarized feeds [40].

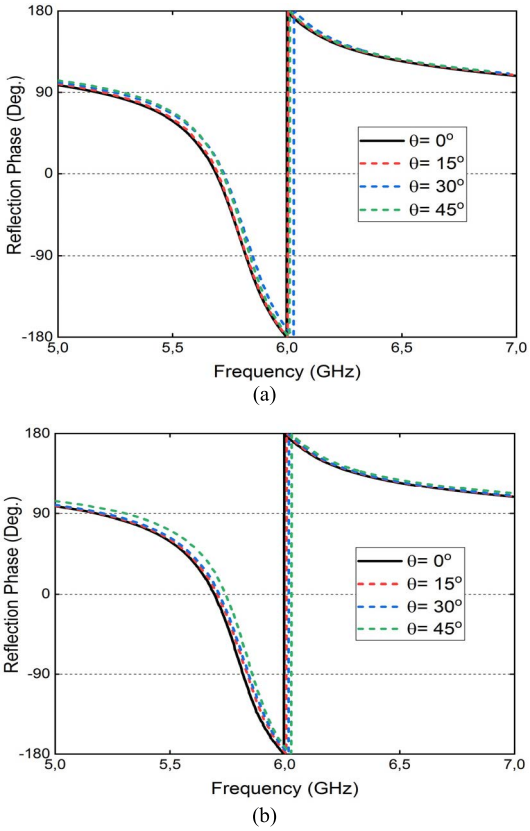

FIGURE 11. (a) Reflection phase variation of the proposed unit cell for different oblique incident angles of O ($\varphi = 0°$ and $\varphi = 90°$) for polarized wave (a) TE, and (b) TM.

The AR response, which is related to cross-polarization can be expressed by [41]:

$$AR = 20 \log_{10} \left(\frac{1+e}{1-e} \right) \tag{5}$$

where $e = 10^{-P_{dB}/20}$ and P_{dB} is the cross-polar power.

The AMC integrated antenna design is illustrated in Fig. 13. It is noticed that a 2 × 2 AMC array size was considered as a reflector to preserve the low-profile characteristic of the overall integrated design. The total footprint of the AMC array is 34.4 × 34.4 mm^2, with a period of 17.2 mm. The separation between the 2 × 2 AMC array and the CP antenna is 3 mm, which is accounted for by means of a foam layer as shown in Fig. 13(a). Furthermore, the fabricated prototype was measured in free space and on the body in the anechoic chamber of National Institute of Scientific Research laboratory (INRS-EMT, Quebec, Canada). The simulated and the measured reflection coefficients (S_{11}) are displayed in Fig. 13(a). A good agreement is observed where the antenna system design is operating in the range of 5.45 to 6.11 GHz, whereas the measured design displayed a wideband resonance ranging from 5.27 to 6.37 GHz.

On the other hand, the simulated and the measured realized gain for the same setup is shown in the left Y-axis scale of Fig. 13(b). It can be observed that, a high gain

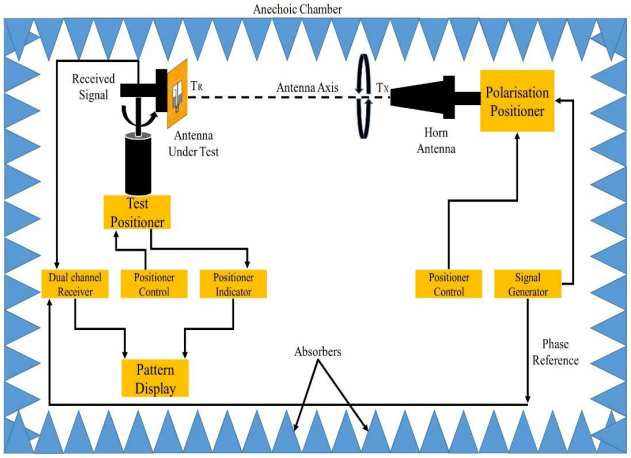

(a)

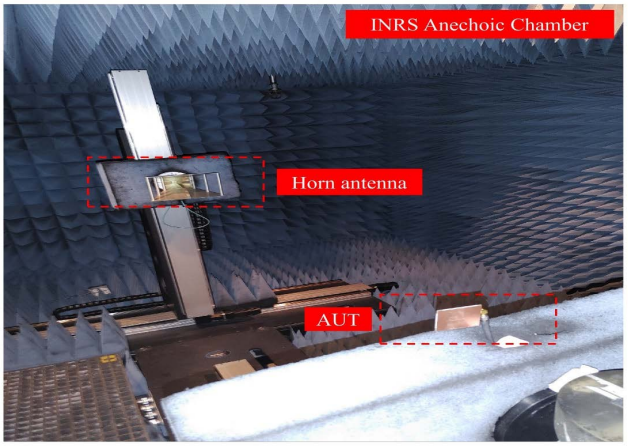

(b)

FIGURE 12. The experimental setup (a) Block diagram of the setup (b) Inside the anechoic chamber.

TABLE 3. Comparison between the antenna design with and without AMC.

With/Without AMC array	Frequency (GHz)	Gain (dBi)	Total Efficiency (%)
Proposed antenna without AMC	5.5	2.94	92.88
	5.7	3.10	97.93
	5.8	3.17	97.68
Proposed Antenna with AMC	5.5	7.15	91.92
	5.7	7.45	98.95
	5.8	7.41	98.49

value is obtained within the band spectrum, due to the AMC arrangement. The AR bandwidth of the proposed antenna covers the same operating range as shown in Fig. 13(b). The simulated 3 dB AR bandwidths are approximately 20% from 5.25 to 5.89 GHz, while the measurement results indicated that the proposed antenna could achieve a bandwidth of 20.5% (5 to 6.2 GHz). Good agreement between the simulated and measured AR curves was observed. Finally, a comparison between the CP antenna without/with AMC array, in terms of realized gain and total efficiency is given in Table 3. It is noted that by adding the AMC array, the gain is increased significantly from 3.18 to 7.41 dBi at 5.8 GHz.

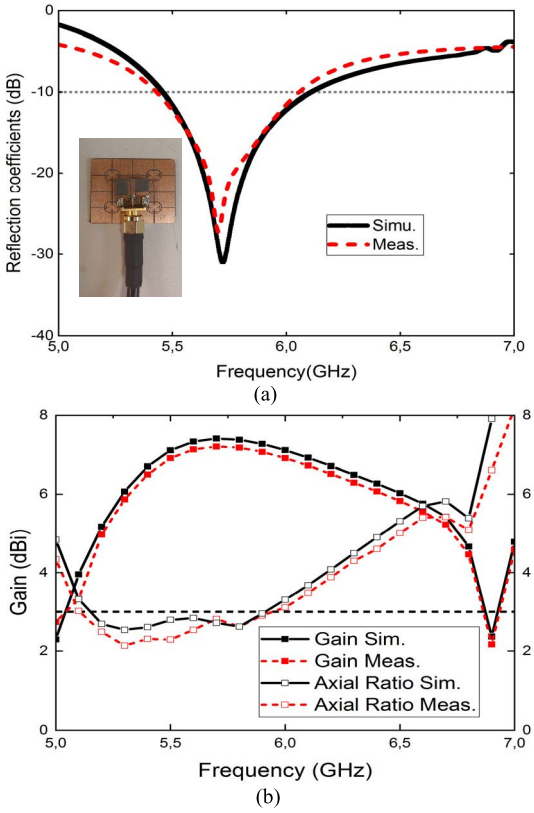

FIGURE 13. Simulated and measured results: (a) reflection coefficients, (b) realized peak gain and axial ratio.

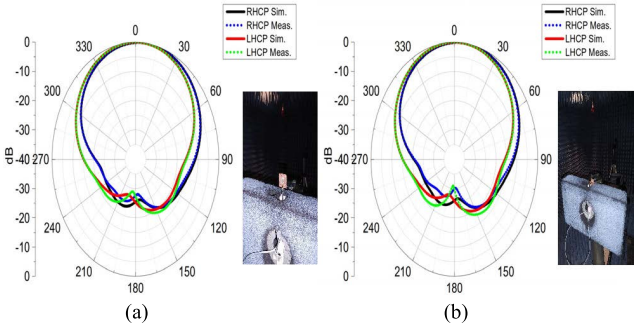

FIGURE 14. Simulated and measured radiation patterns of the proposed antenna design with AMC at 5.8 GHz. (a) $\varphi = 0°$, (b) $\varphi = 90°$.

To validate the proposed concept, Fig. 14 compares the normalized polar plot of the CP antenna with the AMC array in xz ($\varphi = 0°$) and yz ($\varphi = 90°$) plane at 5.8 GHz. From this figure, it can be observed that the radiation patterns of the antenna system are stable unidirectional in the boresight $+z$ direction for RHCP mode, with an agreement between simulated and measured results. In addition, the CP antenna shows a low FBR of 0.59 dB, whereas the integrated design demonstrated an FBR enhancement of 14.13 dB.

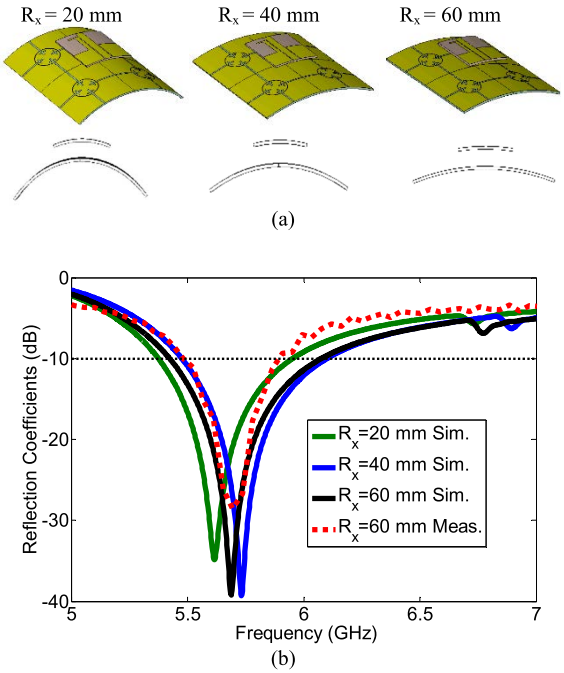

FIGURE 15. Conformal antenna system (a) layout for different values of the curvature radius (b) Simulated and measured reflection coefficients.

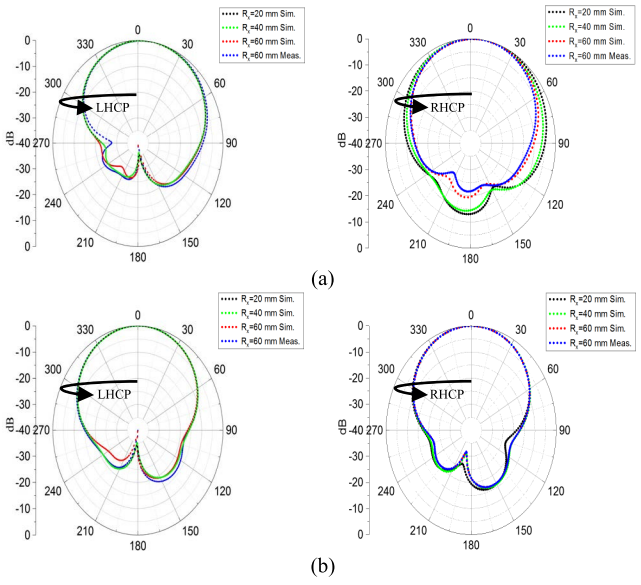

FIGURE 16. Simulated and measured radiation patterns at 5.8 GHz. (a) $\varphi = 0°$, (b) $\varphi = 90°$, respectively.

IV. ANTENNA ANALYSIS

A. EFFECTS OF STRUCTURAL DEFORMATION

In WBAN applications, the wearable antenna must be able to work in conformed conditions when mounted on human body surfaces. Before studying the human body loading effect, we first examine the antenna system performance under different radii of curvature values in free space. Hence, the parameter R_x is used to denote the proposed antenna over cylindrical bending. As shown in Fig. 15(a), the integrated

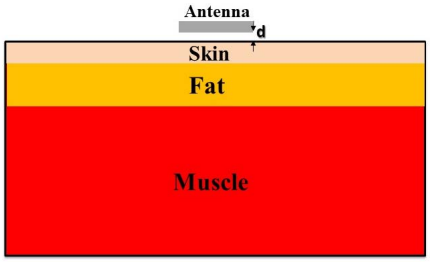

FIGURE 17. Side view of the separation distance d between the proposed antenna and the human tissue model.

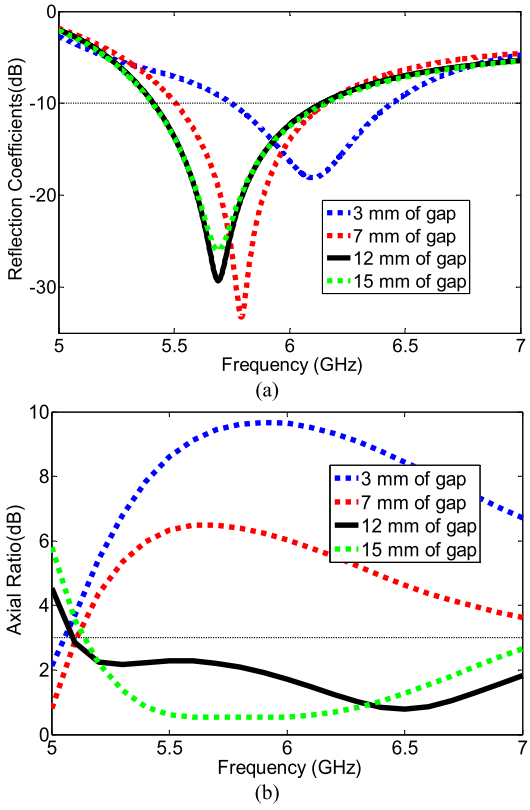

FIGURE 18. Comparison between the proposed antenna distanced by various gaps from human body tissue model, (a) S_{11}, (b) AR.

antenna with three different radii of curvature values, corresponding to 20, 40, and 60 mm along x-axis, were investigated. Bending along the y-axis is not considered for the fact that the surface current is mainly along the y-axis. Thus, bending in this direction will result in more frequency detuning as reported in [42].

A deformed CP antenna prototype is also measured to validate the accuracy of the simulations. The chosen curvatures radii are reasonable representations for different sizes of human arms and legs. Fig. 15(b) shows the simulated and the measured reflection coefficients (S_{11}) of the proposed antenna with three bending radii. We observe that the resonance frequency is maintained below −10 dB for all selected values of R_x. Also, we observe that the resonance frequency is shifted 18 MHz lower when $R_x = 20$ mm. However, when R_x

is increased from 40 to 60 mm, a negligible variation of S_{11} is observed for both cases. In fact, it is observed that the integrated antenna is easily conformed on the cylindrical bending radius, however, the only limiting factor of the operation is the SMA connector zone, for this reason we measured only when $R_X = 60$ mm. From these results, it can be noticed that the proposed prototype has good performances under bending scenarios, which is useful for wearable applications.

TABLE 4. Summary of simulated and measured gain and radiation efficiency for different values of bending radii at 5.8 GHz.

Curvature Radii (mm)	20	40	60	60 Meas.
Gain (dBi)	6.4	6.82	7	6.74
Total Efficiency (dB)	78.57	81.23	83.11	75.06

The simulated and the measured radiation patterns for all antennas are plotted in Fig. 16. Due to the consistency of the simulated radiation patterns, they were verified with a single measurement of the conformal antenna. The antenna gains and efficiency comparisons for the same cases are summarized in Table 4. High gain values of the assembled antenna are achieved even in bending cases. A good agreement is observed between the numerical and experimental results. Small discrepancies were most evident in the lower half-plane axis due to the measurement's setup limitations. Nevertheless, the proposed antenna performance is shown to be robust when compared to previously reported works [26]–[32].

B. SPECIFIC ABSORPTION RATE ANALYSIS

Specific absorption rate (SAR) is a critical parameter for human safety when the antenna is designed to be wearable [43]. The SAR level is determined from eq. (6), where σ is the conductivity of the tissue in S/m, E is the electric field in V/m, and ρ is the mass density of the tissue in kg/m^3.

$$SAR = \frac{\sigma |E|^2}{\rho} \tag{6}$$

In fact, the SAR value should comply with either the US standard of 1.6 W/kg per 1 g of tissue and below of 2 W/kg per 10 g of tissue for EU standard [44]. For off-body performance, a $100 \times 100 \times 33$ mm^3 planar three-layered human tissue is modeled using CST microwave studio, as illustrated in Fig. 17. The model consists of the following layers; 2 mm-thick skin, 8 mm-thick fat, and 23 mm-thick muscle. This is a widely used model to analyze wearable antennas [21]. The gap distance between the antenna ground plane and the human tissue model is referred to as d. The tissues' dielectric properties of each layer of the human tissue model are listed in Table 5 [45], [46]. The absence of a backing reflector between the antenna and the human body, can severely affect the antenna's performance [47].

Fig. 18 indicates the separation distance effects on the antenna parameters in terms of reflection coefficients and

TABLE 5. Human dielectric characteristics at 5.5/5.8 GHz [45], [46].

Tissue	Relative permittivity		Conductivity (S/m)		Loss tangent	
	5.5 GHz	5.8 GHz	5.5 GHz	5.8 GHz	5.5 GHz	5.8 GHz
Dry skin	35.363	35.114	4.983	3.717	1090	1090
Fat	3.463	4.955	0.274	0.293	930	930
Muscle	48.883	48.485	4.609	4.962	1050	1050

AR performances. Analyzing Fig. 18, the CP antenna preserved its resonance and AR performance at a separation of 12 mm from human body tissue. Table 6 summarizes the overall simulated gain values for various gap distances at 5.5 and 5.8 GHz, respectively. It should be mentioned that, the gain values are observed in the main lobe direction of $\theta = 0°$. At the separation of 12 mm, simulated overall gains of 7.35 and 7.33 dBi were achieved at 5.5 and 5.8 GHz, respectively. In addition, enhanced simulated total efficiency was observed, at 12 mm separation cases compared to other separation cases at both frequencies.

TABLE 6. Comparison between the simulated realized gain and the total efficiency for different separation cases.

Separation (mm)	Frequency (GHz)	Realized Gain (dBi)	Total Efficiency (%)
3	5.5	1.46	18.71
	5.8	2.9	26.58
7	5.5	6.9	66.31
	5.8	7.34	76.98
12	5.5	7.35	88.26
	5.8	7.33	84.28
15	5.5	7.14	84.44
	5.8	7.24	90.03

The simulated SAR levels averaged over 1g on the phantom models, at 5.5 and 5.8 GHz are highlighted in Fig. 19. In this study, the calculation was based on the IEEE/IEC 62704-1 standards, with an input power of 100 mW to guarantee accurate benchmarking purposes. High values of 0.29 W/kg and 0.261 W/kg at 5.5 GHz and 5.8 GHz were achieved, respectively. Hence, the proposed antenna at a separation of 12 mm comply with the IEEE/IEC 62704-1 standards overaged over 1g and 10g of tissue. In all results presented above, the proposed antenna operates well under separation distance from the human body of 12 mm. This leads to large sizes, which are not suitable for wearable applications. Thus, incorporating a backing reflector was suggested in the form of an AMC array.

C. HUMAN BODY LOADING

The proposed AMC array provides less backward radiation, thus, the final design should be insensitive to the human body coupling effects. To evaluate this effect, a series of experiments are performed when placed the fabricated

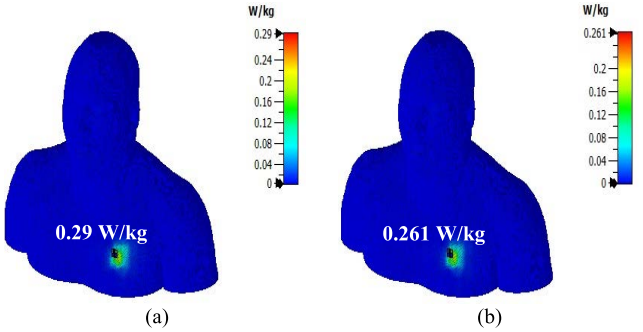

FIGURE 19. SAR of the proposed antenna distanced by a gap of 12 mm (a) 5.5 GHz and (b) 5.8 GHz.

prototype over different human body parts (chest, leg, and arm), as depicted in Fig. 20. As it can be seen, very stable reflection coefficients were maintained for all the measured cases. When placed on the chest, the proposed antenna is operating in the range from 5.37 to 5.98 GHz, where the impedance matching is still maintained in the desired band. This slight discrepancy in the S parameters is due to the highly dielectric and lossy nature of the human body at close proximity distance.

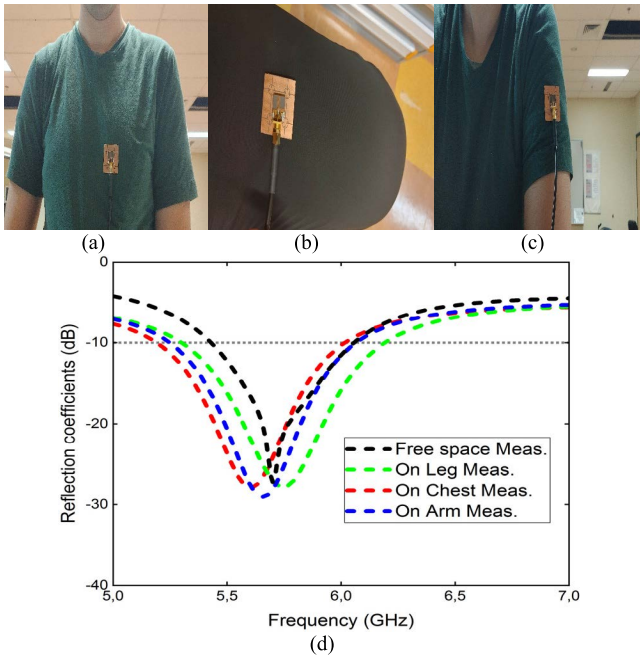

FIGURE 20. 2 × 2 AMC-backed monopole antenna placed on the (a) chest, (b) leg, and (c) arm of a realistic human body numerical phantom to evaluate the radiation characteristics presented in terms of (d) measured reflection coefficients.

To match the measurement results presented in Fig. 20(d), a full-wave electromagnetic simulation with a realistic heterogeneous (Hugo) voxel human body phantom was used to analyze the radiation performance of the proposed antenna. The heterogeneous model is composed of 32 different tissues types with a mesh size of $1 \times 1 \times 1$ mm^3 (male, 113 kg weight, 187 cm height, 38 years old) [48]. The integrated design was placed at three different positions on the HUGO model, including the chest, arm, and leg, respectively, as illustrated in the top row of Fig. 21(a)-(c).

TABLE 7. Comparison between loaded human body CP antenna without and with AMC in terms of gain, FBR and efficiency.

With/Without AMC array	Frequency (GHz)	Gain (dBi)	FBR (dB)	Total Efficiency (%)
Proposed antenna alone (12 mm separation)	5.5	7.11	33.01	84.47
	5.7	7.41	33.41	89.08
	5.8	7.38	33.40	88.47
Integrated design mounted on Arm	5.5	6.89	30.48	90.66
	5.7	6.51	28.50	81.9
	5.8	6.24	28.29	76.03
Integrated design mounted on Chest	5.5	7.38	30.16	87.13
	5.7	7.39	31.72	88.02
	5.8	7.47	31.38	85.64
Integrated design mounted on Leg	5.5	7.32	30.98	92.81
	5.7	7.29	34.24	94.69
	5.8	7.05	35.20	91.85

TABLE 8. Level of the proposed antenna at 5.8 GHZ.

Unit (W/kg)	Standard	On Chest	On Arm	On Leg
1 g average (U. S.)	1.6	0.2077	0.0872	0.0264
10 g average (EUR.)	2	0.1372	0.0481	0.0144

To reduce the simulation time, a reasonably sized portion of Hugo's body was selected for the simulation instead of simulating the proposed antenna on the entire numerical body model. In all the studied scenarios, the antenna was assumed to be separated from the body by a foam spacer with a thickness of 3 mm. After readjusting the off-body antenna orientation, the simulated radiation patterns of the proposed antenna were performed (as shown in the middle row of Fig. 21(d)-(e)). It can be seen that the proposed antenna in contact with Hugo voxel displayed a lower back-radiation for all three cases, due to the unidirectional radiation pattern type. The realized gain and the axial ratio characterizations, in free space and on-body for the same setup, are presented in the lower row of Fig. 21(f). A higher front-to-back ratio of the antenna is observed for all three cases, where the body acts as an extension on the ground plane. This increase affected the peak gain of the proposed antenna. The gain of the antenna is within the range of 6.89 to 7.84 dBi and the 3dB-AR characteristics remained unchanged from 4.9 to 6.1 GHz.

In addition, Table 7 shows a comparison of the simulated gain, FBR, and the efficiency values for all cases. It is noted that the gain values were taken in the main lobe direction of $\theta = 0°$. The proposed antenna exhibited high gain values when operating near to the human body model. To recall, the rationale behind the high gain values of the proposed antenna alone at separation of 12 mm is based on the fact that

TABLE 9. Comparison of the proposed antenna and some other wearable antennas applied in the 2.4/5GHz WBAN band in terms of gain, FBR, maximum SAR and radiation efficiency.

Ref.	Dimensions	BW (%)	Axial Ratio (%)	Gain (dBi)	FBR (dB)	Rad. Effi. (%)	SAR (Kg/m^3)	Num. of unit cells	Flexible
[18]	86 × 86 × 3.62 1.00 λ_0×1.00 λ_0×0.042 λ_0 (Area 1 λ_0^2)	7.77	LP	6.634	25	91.05	0.333	4×4	No
[19]	68 × 38 × 5 0.56 λ_0×0.31 λ_0×0.054 λ_0 (Area 0.174 λ_0^2)	4.88	LP	6.88	-	67.48	0.244	2×1	Yes
[20]	81 × 81 × 4 0.62 λ_0×0.62 λ_0×0.030 λ_0 (Area 0.384 λ_0^2)	14.7	LP	7.3	17	70	0.554	3×3	No
[24]	89 × 83 × 9.2855 0.71 λ_0×0.66 λ_0×0.074 λ_0 (Area 0.469 λ_0^2)	6.98	LP	6.4	-	-	0.29	3×3	Yes
[26]	55 × 55 × 5.2 0.44 λ_0×0.44 λ_0×0.04 λ_0 (Area 0.194 λ_0^2)	4.5	2.4	4.7	17.5	58	0.54	-	No
[27]	100 × 100 × 12 1.82 λ_0×1.82 λ_0×0.129 λ_0 (Area 3.312 λ_0^2)	11.8	6.4	3.5	-	79.9	-	-	No
[28]	178 × 178 × 14.448 3.06 λ_0×3.06 λ_0×0.249 λ_0 (Area 9.364 λ_0^2)	18.3	18.3	6.2	-	90	0.131	1×1	No
[29]	35 × 35 × 2.24 0.68 λ_0×0.68 λ_0×0.044 λ_0 (Area 0.462 λ_0^2)	6.6	3.85	7.2	-	-	0.613	-	Yes
[30]	50 × 50 × 5.5 0.41 λ_0×0.41 λ_0×0.045 λ_0 (Area 0.168 λ_0^2)	10.78	2.72	5.2	-	79	0.18	4×4	Yes
[31]	60 × 60 × 15 1.5 λ_0×1.5 λ_0×0.37 λ_0 (Area 2.25 λ_0^2)	20.7	9.6	5	-	-	0.237	-	Yes
[32]	85.5 × 85.5 × 5.62 0.68 λ_0×0.68 λ_0×0.04 λ_0 (Area 0.462 λ_0^2)	7.6	10.3	1.98	16.7	83	0.71	3×3	Yes
[38]	65.7 × 65.7 × 4.7 1.25 λ_0×1.25 λ_0×0.089 λ_0 (Area 1.563 λ_0^2)	18	LP	4.8	8	-	0.683	3×3	Yes
[49]	130.8 × 130.8 × 10.15 0.68 λ_0×0.68 λ_0×0.053 λ_0 (Area 0.462 λ_0^2)	0.736	0.7	5.03	24.5	70	0.0433	4×4	Semi-flex
[50]	56 × 56 × 3.27 0.46 λ_0×0.46 λ_0×0.027 λ_0 (Area 0.209 λ_0^2)	7.23	LP	6.51	11.4	74.8	0.22	2×2	No
[51]	42 × 28 × 4 0.77 λ_0×0.51 λ_0×0.073 λ_0 (Area 0.393 λ_0^2)	17.31	LP	6.7	-	77	0.3699	3×2	Yes
[52]	72 × 72 × 6.05 0.59 λ_0×0.59 λ_0×0.049 λ_0 (Area 0.348 λ_0^2)	7.14	LP	6.2	15	76.74	5.17	6×6	Yes
[53]	62 × 42 × 4 0.5 λ_0×0.3 λ_0×0.028 λ_0 (Area 0.15 λ_0^2)	5.5	LP	6.2	23	-	0.66	2×2	Yes
[25]	50 × 50 × 9.5 0.4 λ_0×0.4 λ_0×0.076 λ_0 (Area 0.16 λ_0^2)	1.84	LP	4.78	12	78.97	0.714 (10g)	4×4	Yes
[54]	46 × 46 × 5.74 0.86 λ_0×0.86 λ_0×0.109 λ_0 (Area 0.740 λ_0^2)	63.5	LP	7.5	16.4	83.8	1.6	5×5	Yes
Proposed	34.4 × 34.4 × 4.016 0.62 λ_0×0.62 λ_0×0.073 λ_0 (Area 0.384 λ_0^2)	11.44	18.18	7.6	35.2	94.69	0.0264	2×2	Semi-flex

the human tissue acted as a reflector. This demonstrates the suitability of the integrated design for wearable applications.

Fig. 22 shows the simulated 1 g averaged SAR levels due to the proposed antenna for the three cases. As a benchmark,

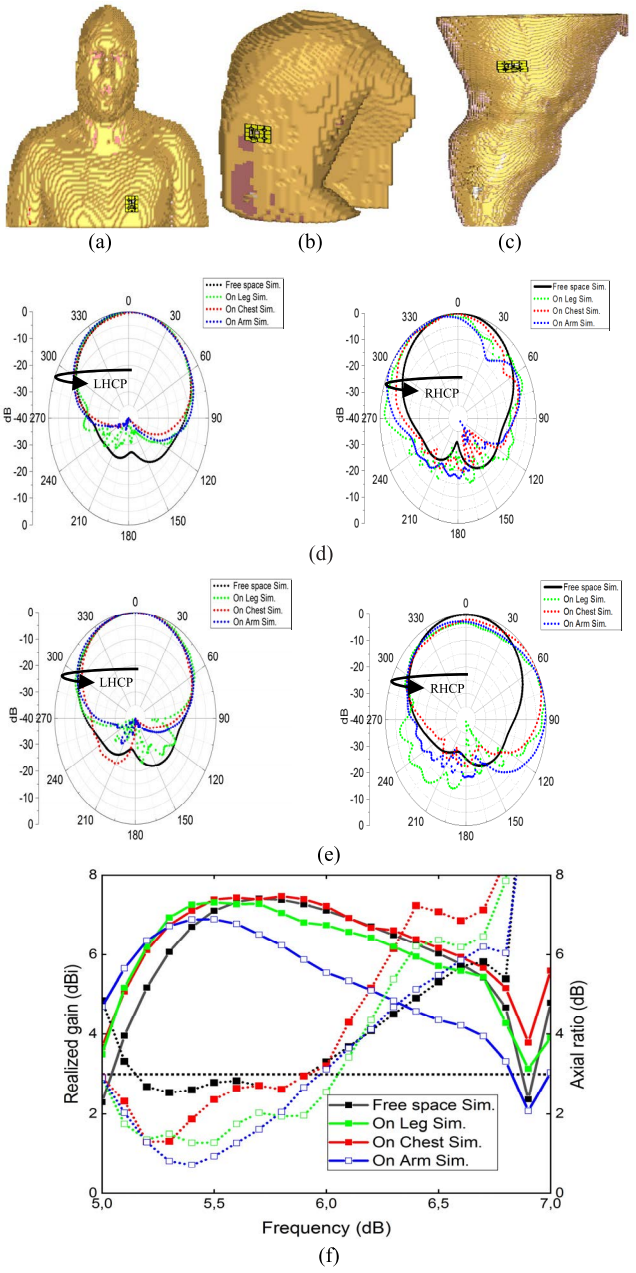

FIGURE 21. 2 × 2 AMC-backed monopole antenna placed on the (a) chest, (b) arm, and (c) leg of a realistic human body numerical phantom to evaluate the radiation characteristics presented in terms of radiation patterns at 5.8 GHz along the (d) $\varphi = 0°$, (e) $\varphi = 90°$. (f) Antenna realized gain and axial ratio.

a power level of 100 mW accepted by the proposed antenna was chosen to evaluate the SAR performance. The maximum SAR level recorded was 0.2077 W/kg, 0.0872 W/kg, and 0.0264 W/kg, on the chest, arm, and leg, respectively. The simulated averaged SAR values over 1 g and 10 g of tissues for the three cases, are summarized in Table 8. These values are not only well below both US and EU standards, but also much smaller than those reported in the literature [18]–[54].

Finally, Table 9 compares the performance of the proposed design and the recent state-of-the-art antennas reported in the literature. It can be noted that the antennas [18]–[54] are linearly polarized (LP), which could lead to unreliable wireless links due to the polarization mismatch caused by the constant human body motion. In [26]–[28], although those antennas achieved CP radiation, they were based on rigid substrates. However, compared with the reported flexible CP antennas applied for WBAN applications, the proposed antenna has the advantages of compactness, conformability, higher gain, efficiency, wider AR bandwidth, and lowest SAR values.

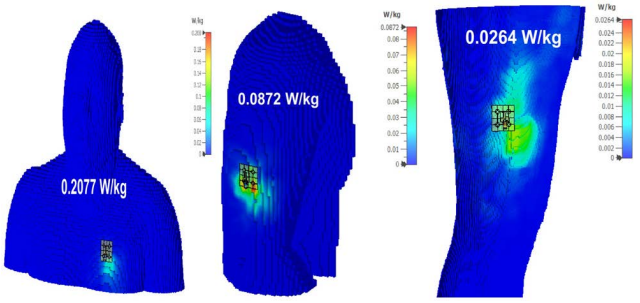

FIGURE 22. Simulated 1 g averaged SAR values of the integrated CP patch antenna mounted on (a) the chest, (b) the arm, and (c) the leg of the HUGO human body model in CST MWS at 5.8 GHz.

V. CONCLUSION

In this paper, a compact flexible 2 × 2 AMC-backed planar CP monopole antenna for wearable applications has been proposed. The antenna design is based on a simple topology structure to generate a wide-band broadside CP radiation. The antenna with and without the AMC reflector enables good impedance matching in free space. Meanwhile, good performance was achieved, while loading the CP antenna at a separation distance of 12 mm from the human body model, which leads to an increase in the overall size. To minimize the separation distance and the effects of the human body on the antenna performances, a 2 × 2 AMC array is designed to form the antenna's backplane, and also yields toward enhancing the radiation performance. Due to using the CP approach for the antenna design, the proposed work radiator size is highly compact with a size reduction of 25% compared to recently reported works. Moreover, full-wave simulations and experimental measurements demonstrated the robustness of the assembled design for different bending conditions and human-body loading effects. The antenna system was also shown to be effective in reducing EM absorption in the human body model. With all these features, the proposed antenna is highly suitable for wearable applications.

ACKNOWLEDGMENT

The authors would like to thank Tayeb A. Denidni and Dr. Arun Kesavan from the National Institute of Scientific Research (INRS-EMT) Laboratory, University of Quebec, Quebec, Canada, for providing the measuring radiation pattern facilities.

REFERENCES

[1] P. S. Hall and Y. Hao, *Antennas and Propagation for Body-Centric Wireless Communications*. Norwood, MA, USA: Artech House, 2012.

[2] A. Tsolis, W. G. Whittow, A. A. Alexandridis, and J. Vardaxoglou, "Embroidery and related manufacturing techniques for wearable antennas: Challenges and opportunities," *Electronics*, vol. 3, no. 2, pp. 314–338, May 2014.

[3] U. Ullah, M. Al-Hasan, S. Koziel, and I. B. Mabrouk, "Circular polarization diversity implementation for correlation reduction in wideband low-cost multiple-input-multiple-output antenna," *IEEE Access*, vol. 8, pp. 95585–95593, 2020.

[4] M. Sarestoniemi, C. Pomalaza-Raez, C. Kissi, and J. Iinatti, "Simulation and measurement data-based study on fat as propagation medium in WBAN abdominal implant communication systems," *IEEE Access*, vol. 9, pp. 46240–46259, 2021.

[5] K. Zhang, G. A. E. Vandenbosch, and S. Yan, "A novel design approach for compact wearable antennas based on metasurfaces," *IEEE Trans. Biomed. Circuits Syst.*, vol. 14, no. 4, pp. 918–927, Aug. 2020.

[6] D. Yang, J. Hu, and S. Liu, "A low profile UWB antenna for WBAN applications," *IEEE Access*, vol. 6, pp. 25214–25219, 2018.

[7] M. R. I. Faruque, M. I. Hossain, and M. T. Islam, "Low specific absorption rate microstrip patch antenna for cellular phone applications," *IET Microw., Antennas Propag.*, vol. 9, no. 14, pp. 1540–1546, Nov. 2015.

[8] L. A. Y. Poffelie, P. J. Soh, S. Yan, and G. A. E. Vandenbosch, "A high-fidelity all-textile UWB antenna with low back radiation for off-body WBAN applications," *IEEE Trans. Antennas Propag.*, vol. 64, no. 2, pp. 757–760, Feb. 2016.

[9] Y. J. Li, Z. Y. Lu, and L. S. Yang, "CPW-fed slot antenna for medical wearable applications," *IEEE Access*, vol. 7, pp. 42107–42112, 2019.

[10] S. Agneessens and H. Rogier, "Compact half diamond dual-band textile HMSIW on-body antenna," *IEEE Trans. Antennas Propag.*, vol. 62, no. 5, pp. 2374–2381, May 2014.

[11] S. Agneessens, S. Lemey, T. Vervust, and H. Rogier, "Wearable, small, and robust: The circular quarter-mode textile antenna," *IEEE Antennas Wireless Propag. Lett.*, vol. 14, pp. 1482–1485, 2015.

[12] S. Yan, P. J. Soh, and G. A. E. Vandenbosch, "Dual-band textile MIMO antenna based on substrate-integrated waveguide (SIW) technology," *IEEE Trans. Antennas Propag.*, vol. 63, no. 11, pp. 4640–4647, Nov. 2015.

[13] A. Arif, M. Zubair, M. Ali, M. U. Khan, and M. Q. Mehmood, "A compact, low-profile fractal antenna for wearable on-body WBAN applications," *IEEE Antennas Wireless Propag. Lett.*, vol. 18, no. 5, pp. 981–985, May 2019.

[14] P. J. Soh, G. A. E. Vandenbosch, S. L. Ooi, and M. R. N. Husna, "Wearable dual-band Sierpinski fractal PIFA using conductive fabric," *Electron. Lett.*, vol. 47, no. 6, pp. 365–367, Mar. 2011.

[15] W. El Hajj, C. Person, and J. Wiart, "A novel investigation of a broadband integrated inverted-F antenna design; application for wearable antenna," *IEEE Trans. Antennas Propag.*, vol. 62, no. 7, pp. 3843–3846, Jul. 2014.

[16] H. Xiaomu, S. Yan, and G. A. E. Vandenbosch, "Wearable button antenna for dual-band WLAN applications with combined on and off-body radiation patterns," *IEEE Trans. Antennas Propag.*, vol. 65, no. 3, pp. 1384–1387, Mar. 2017.

[17] Y. B. Chaouche, M. Nedil, I. Benmabrouk, and M. Belazzoug, "A dual-band antenna backed by AMC surface using genetic algorithm for 2.4/5.8 GHz underground mining communications," in *Proc. IEEE AP-S/URSI Conf.*, Montreal, QC, Canada, Jul. 2020, pp. 929–930.

[18] M. El Atrash, M. A. Abdalla, and H. M. Elhennawy, "A wearable dual-band low profile high gain low SAR antenna AMC-backed for WBAN applications," *IEEE Trans. Antennas Propag.*, vol. 67, no. 10, pp. 6378–6388, Oct. 2019.

[19] M. A. B. Abbasi, S. S. Nikolaou, M. A. Antoniades, M. N. Stevanović, and P. Vryonides, "Compact EBG-backed planar monopole for BAN wearable applications," *IEEE Trans. Antennas Propag.*, vol. 65, no. 2, pp. 453–463, Feb. 2017.

[20] G.-P. Gao, B. Hu, S.-F. Wang, and C. Yang, "Wearable circular ring slot antenna with EBG structure for wireless body area network," *IEEE Antennas Wireless Propag. Lett.*, vol. 17, no. 3, pp. 434–437, Mar. 2018.

[21] Y. S. Chen and T.-Y. Ku, "A low-profile wearable antenna using a miniature high impedance surface for smartwatch applications," *IEEE Antennas Wireless Propag. Lett.*, vol. 15, pp. 1144–1147, 2016.

[22] N. M. Hicho, E. A. Daviu, M. C. S. Fabr, M. Ferrando-Bataller, and D. S. Escuderos, "Wideband high-impedance surface reflector for low-profile high-gain UHF antenna," in *Proc. 9th Eur. Conf. Antennas Propag. (EuCAP)*, Lisbon, Portugal, 2015, pp. 1–4.

[23] Y. B. Chaouche, M. Nedil, M. Elbadawe, M. Olaimat, and O. Ramahi, "Wearable metasurface antenna based on electrically-small ring resonators for WBAN applications," *IET Electron. Lett.*, vol. 51, no. 1, pp. 4–7, 2021.

[24] S. M. Saeed, C. A. Balanis, C. R. Birtcher, A. C. Durgun, and H. N. Shaman, "Wearable flexible reconfigurable antenna integrated with artificial magnetic conductor," *IEEE Antennas Wireless Propag. Lett.*, vol. 16, pp. 2396–2399, 2017.

[25] K. Agarwal, Y.-X. Guo, and B. Salam, "Wearable AMC backed near-endfire antenna for on-body communications on latex substrate," *IEEE Trans. Compon., Packag., Manuf. Technol.*, vol. 6, no. 3, pp. 346–358, Mar. 2016.

[26] Z. H. Jiang, M. D. Gregory, and D. H. Werner, "Design and experimental investigation of a compact circularly polarized integrated filtering antenna for wearable biotelemetric devices," *IEEE Trans. Biomed. Circuits Syst.*, vol. 10, no. 2, pp. 328–338, Apr. 2016.

[27] X. Hu, S. Yan, and G. A. E. Vandenbosch, "Compact circularly polarized wearable button antenna with broadside pattern for U-NII worldwide band applications," *IEEE Trans. Antennas Propag.*, vol. 67, no. 2, pp. 1341–1345, Feb. 2019.

[28] U. Ullah, I. B. Mabrouk, and S. Koziel, "A compact circularly polarized antenna with directional pattern for wearable off-body communications," *IEEE Antennas Wireless Propag. Lett.*, vol. 18, no. 12, pp. 2523–2527, Dec. 2019.

[29] H. C. Yang, X. Y. Liu, Y. Fan, and M. M. Tentzeris, "Flexible circularly polarized antenna with axial ratio bandwidth enhancement for off-body communications," *IET Microw., Antennas Propag.*, vol. 15, no. 7, pp. 754–767, Jun. 2021.

[30] Z. H. Jiang, Z. Cui, T. Yue, Y. Zhu, and D. H. Werner, "Compact, highly efficient, and fully flexible circularly polarized antenna enabled by silver nanowires for wireless body-area networks," *IEEE Trans. Biomed. Circuits Syst.*, vol. 11, no. 4, pp. 920–932, Aug. 2017.

[31] U. Illahi, J. Iqbal, M. I. Sulaiman, M. M. Alam, M. M. Su'Ud, M. H. Jamaluddin, and M. N. M. Yasin, "Design of new circularly polarized wearable dielectric resonator antenna for off-body communication in WBAN applications," *IEEE Access*, vol. 7, pp. 150573–150582, 2019.

[32] R. Joshi, E. F. N. M. Hussin, P. J. Soh, M. F. Jamlos, H. Lago, A. A. Al-Hadi, and S. K. Podilchak, "Dual-band, dual-sense textile antenna with AMC backing for localization using GPS and WBAN/WLAN," *IEEE Access*, vol. 8, pp. 89468–89478, 2020.

[33] C. Nguyen and K. Chang, *Analysis Methods for RF, Microwave, and Millimeter-Wave Planar Transmission Line Structures*. Hoboken, NJ, USA: Wiley, 2000.

[34] U. Ullah and S. Koziel, "A novel coplanar-strip-based excitation technique for design of broadband circularly polarization antennas with wide 3 dB axial ratio beamwidth," *IEEE Trans. Antennas Propag.*, vol. 67, no. 6, pp. 4224–4229, Jun. 2019.

[35] S. K. K. Dash, Q. S. Cheng, and T. Khan, "An off-center-fed compact wideband antenna with truncated corners and parasitic patches for circular polarization," *Int. J. RF Microw. Comput.-Aided Eng.*, vol. 30, no. 8, Aug. 2020, Art. no. e22244.

[36] *CST Microwave Studio*, Comput. Simul. Technol., Darmstadt, Germany, 2020.

[37] Y. Sung, "Bandwidth enhancement of a microstrip line-fed printed wide-slot antenna with a parasitic center patch," *IEEE Trans. Antennas Propag.*, vol. 60, no. 4, pp. 1712–1716, Apr. 2012.

[38] H. R. Raa, A. I. Abbosh, H. M. Al-Rizzo, and D. G. Rucker, "Flexible and compact AMC based antenna for telemedicine applications," *IEEE Trans. Antennas Propag.*, vol. 61, no. 2, pp. 524–531, Feb. 2013.

[39] H. Malekpoor and S. Jam, "Improved radiation performance of low profile printed slot antenna using wideband planar AMC surface," *IEEE Trans. Antennas Propag.*, vol. 64, no. 11, pp. 4626–4638, Nov. 2016.

[40] Y. T. Lo and S. W. Lee, *Antenna Handbook: Theory, Applications, and Design*. Boston, MA, USA: Springer, 2013.

[41] B. Y. Toh, R. Cahill, and V. F. Fusco, "Understanding and measuring circular polarization," *IEEE Trans. Educ.*, vol. 46, no. 3, pp. 313–318, Aug. 2003.

[42] S. Yan, L. A. Y. Poffelie, P. J. Soh, X. Zheng, and G. A. E. Vandenbosch, "On-body performance of wearable UWB textile antenna with full ground plane," in *Proc. 10th Eur. Conf. Antennas Propag. (EuCAP)*, Apr. 2016, pp. 5–8.

[43] *Human Exposure to Radio Frequency Fields From Hand-Held and Body-Mounted Wireless Communication Devices-Human Models*, Standard IEC 62209, Instrumentation and Procedures, 2010.
[44] *IEEE Standard for Safety Levels With Respect to Human Exposure to Radio Frequency Electromagnetic Fields, 3 kHz to 300 GHz*, IEEE Standard C95.1-2005, 2007.
[45] *Dielectric Properties of Body Tissues*. Accessed: Jun. 15, 2018. [Online]. Available: http://niremf.ifac.cnr.it/tissprop/
[46] *Body Tissue Dielectric Parameters*. Accessed: Jun. 15, 2018. [Online]. Available: https://www.fcc.gov/general/body-tissue-dielectricparameters
[47] D. M. N. Elsheakh, A. M. Soliman, and E. A. Abdallah, "Low specific absorption rate hexa-band coplanar waveguide-fed planar inverted-F antenna with independent resonant frequency control for wireless communication applications," *IET Microw., Antennas Propag.*, vol. 8, no. 4, pp. 207–216, Mar. 2014.
[48] E. Gjonaj, M. Bartsch, M. Clemens, S. Schupp, and T. Weiland, "High-resolution human anatomy models for advanced electromagnetic field computations," *IEEE Trans. Magn.*, vol. 38, no. 2, pp. 357–360, Mar. 2002.
[49] K. N. Paracha, S. K. A. Rahim, P. J. Soh, M. R. Kamarudin, K.-G. Tan, Y. C. Lo, and M. T. Islam, "A low profile, dual-band, dual polarized antenna for indoor/outdoor wearable application," *IEEE Access*, vol. 7, pp. 33277–33288, 2019.
[50] M. El Atrash, M. A. Abdalla, and H. M. Elhennawy, "A compact highly efficient Π-section CRLH antenna loaded with textile AMC for wireless body area network applications," *IEEE Trans. Antennas Propag.*, vol. 69, no. 2, pp. 648–657, Feb. 2021.
[51] G.-P. Gao, C. Yang, B. Hu, R.-F. Zhang, and S.-F. Wang, "A wearable PIFA with an all-textile metasurface for 5 GHz WBAN applications," *IEEE Antennas Wireless Propag. Lett.*, vol. 18, no. 2, pp. 288–292, Feb. 2019.
[52] S. X. Ta and I. Park, "Dual-band low-profile crossed asymmetric dipole antenna on dual-band AMC surface," *IEEE Antennas Wireless Propag. Lett.*, vol. 13, pp. 587–590, 2014.
[53] Z. H. Jiang, D. E. Brocker, P. E. Sieber, and D. H. Werner, "A compact, low-profile metasurface-enabled antenna for wearable medical body-area network devices," *IEEE Trans. Antennas Propag.*, vol. 62, no. 8, pp. 4021–4030, Aug. 2014.
[54] X. Y. Liu, Y. H. Di, H. Liu, Z. T. Wu, and M. M. Tentzeris, "A planar windmill-like broadband antenna equipped with artificial magnetic conductor for off-body communications," *IEEE Antennas Wireless Propag. Lett.*, vol. 15, pp. 64–67, 2016.

YOUCEF BRAHAM CHAOUCHE (Graduate Student Member, IEEE) received the B.A.Sc., M.A.Sc., and Ph.D. degrees in electrical engineering from the Université of Mohamed El Bachir El Ibrahimi de Bordj Bou Arréridj, Algeria, in 2011, 2013, and 2019, respectively. He is currently pursuing the Ph.D. degree in electrical and computer engineering with the University of Quebec at Abitibi-Temiscamingue, QC, Canada. His current research interests include implantable and wearable antenna design, conformal and reconfigurable antennas, genetic algorithms and evolutionary computation, machine learning, and wireless body area network for medical applications. He was a recipient of the FRQNT International Internship Program, in 2020, and FUQAT Award for the International Students, in 2021.

MOURAD NEDIL (Senior Member, IEEE) received the Dipl. (Ing.) degree from the University of Algiers (USTHB), Algiers, Algeria, in 1996, the D.E.A. (M.S.) degree from the University of Marne la Vallée, Marne la Vallée, France, in 2000, and the Ph.D. degree from the Institut National de la Recherche Scientifique (INRS-EMT), Université de Québec, Montreal, QC, Canada, in April 2006. He received a Postdoctoral Fellowship from the INRS-EMT, RF Communications Systems Group, from 2006 to 2008. In June 2008, he joined the Engineering School Department, University of Quebec at Abitibi-Témiscamingue, QC, Canada, where he is currently a Full Professor. His research interests include antennas, MIMO radio-wave propagation, and microwave devices.

ISMAIL BEN MABROUK (Senior Member, IEEE) received the B.A.Sc. and M.A.Sc. degrees in electrical engineering from the University of Lille, Lille, France, in 2006 and 2007, respectively, and the Ph.D. degree in electrical engineering from the University of Quebec, Canada, in 2012. From 2007 to 2009, he was with Huawei Technologies, Paris, France. In 2012, he joined the Wireless Devices and Systems (WiDeS) Group, University of Southern California, Los Angeles, USA. He is currently an Assistant Professor with Durham University, Durham, U.K. His research interests include implantable and wearable antenna design, propagation studies for multiple-input and multiple-output (MIMO) systems at the millimiter-wave and THz frequencies, deep learning, and wireless body area network for medical applications. He was a recipient of the Abu Dhabi Award for Research Excellence (AARE).

OMAR M. RAMAHI (Fellow, IEEE) was born in Jerusalem, Palestine. He received the B.S. degree (Hons.) in mathematics and electrical and computer engineering from Oregon State University, Corvallis, OR, USA, and the M.S. and Ph.D. degrees in electrical and computer engineering from the University of Illinois at Urbana–Champaign, Champaign, IL, USA. He was with Digital Equipment Corporation (currently HP), MA, USA, where he was a member of the Alpha Server Product Development Group. In 2000, he joined the Faculty of the James Clark School of Engineering, University of Maryland, College Park, MD, USA, as an Assistant Professor and later as a tenured Associate Professor, where he was also a Faculty Member of the CALCE Electronic Products and Systems Center. He is currently a Professor with the Department of Electrical and Computer Engineering, University of Waterloo, Waterloo, ON, Canada. He has authored or coauthored over 450 journal and conference technical articles on topics related to the electromagnetic phenomena and computational techniques. He has coauthored the book *EMI/EMC Computational Modeling Handbook* (1st Edition: Kluwer, 1998; 2nd Edition: Springer-Verlag, 2001; Japanese Edition, in 2005). He received the 2004 University of Maryland Pi Tau Sigma Purple Cam Shaft Award. He also received the Excellent Paper Award from the 2004 International Symposium on Electromagnetic Compatibility, Sendai, Japan, and the 2010 University of Waterloo Award for Excellence in Graduate Supervision. In 2012, he was a recipient of the IEEE EMC Society Technical Achievement Award.